CHEMISTRY

Evoking ordered vacancies in metallic nanostructures toward a vacated Barlow packing for high-performance hydrogen evolution

Zhicheng Zhang[1,2]*, Guigao Liu[3]*, Xiaoya Cui[2]*, Yue Gong[4,5,6]*, Ding Yi[7]*, Qinghua Zhang[4,5,6],
Chongzhi Zhu[8,9], Faisal Saleem[3], Bo Chen[3], Zhuangchai Lai[3], Qinbai Yun[3], Hongfei Cheng[2],
Zhiqi Huang[3], Yongwu Peng[2,10], Zhanxi Fan[3,11], Bing Li[12], Wenrui Dai[13,14,15], Wei Chen[13,14,15],
Yonghua Du[16], Lu Ma[16], Cheng-Jun Sun[17], Inhui Hwang[17], Shuangming Chen[18], Li Song[18],
Feng Ding[7,19]†, Lin Gu[4,5,6]†, Yihan Zhu[8,9]†, Hua Zhang[3,11]†

Metallic nanostructures are commonly densely packed into a few packing variants with slightly different atomic packing factors. The structural aspects and physicochemical properties related with the vacancies in such nanostructures are rarely explored because of lack of an effective way to control the introduction of vacancy sites. Highly voided metallic nanostructures with ordered vacancies are however energetically high lying and very difficult to synthesize. Here, we report a chemical method for synthesis of hierarchical Rh nanostructures (Rh NSs) composed of ultrathin nanosheets, composed of hexagonal close-packed structure embedded with nanodomains that adopt a vacated Barlow packing with ordered vacancies. The obtained Rh NSs exhibit remarkably enhanced electrocatalytic activity and stability toward the hydrogen evolution reaction (HER) in alkaline media. Theoretical calculations reveal that the exceptional electrocatalytic performance of Rh NSs originates from their unique vacancy structures, which facilitate the adsorption and dissociation of H_2O in the HER.

INTRODUCTION

A vacancy is defined as a type of point defect existing intrinsically in nearly all crystalline nanomaterials (1). It usually refers to the removal of oppositely charged ions in the lattice of ionic crystals or neutral atoms in the lattice of metals as "Schottky defects," without perturbing the electrical equilibrium of the whole structures.

Vacancies are fundamentally important because they are closely related to many physicochemical properties of nanomaterials, such as electric, mechanical, thermal, optical, magnetic, and catalytic properties (2–5), which have been intensively investigated in many ionic crystalline nanomaterials. Metallic nanostructures that manifest themselves as excellent examples for the sphere packing problem are rarely studied with respect to the formation and property of vacancies. This is because metallic nanostructures are densely packed, either in densest-packing forms with an atomic packing factor (APF) of $\pi/\sqrt{18}$ as proposed by Barlow [i.e., Barlow packing, including polytypes like cubic close packing [also called face-centered cubic (FCC)], hexagonal close packing (HCP; 4H, 6H, etc.), or other packing variants with slightly smaller APFs [e.g., body-centered cubic, body-centered tetragonal, or face-centered tetragonal (FCT)] (6). The latter packing modes differ from the densest packing only by a small energy difference, among which the phase transformation, as one kind of strategies for phase engineering of nanomaterials (7), could be readily triggered by external stimuli such as temperature, pressure, or chemical environment (8–10). However, directly creating vacancy sites in metallic nanostructures is very challenging due to the large energy deviation of vacated nanostructures from those densest-packed ground-state geometries. Most vacancy sites appearing in monometallic nanostructures are generated by thermal equilibrium with an extremely small population (e.g., 10^{-8} to 10^{-4}) (11), which are dynamic, disordered, and difficult to directly characterize. To unravel the correlation between structure and property of vacancies in metallic nanostructures requires the introduction of a considerable quantity of vacancies at symmetry-equivalent sites to form orderly vacated structures.

Electrocatalytic reactions are highly structure sensitive, especially when catalyzed by metallic nanostructures (12, 13). Even with an identical APF diverse densest Barlow packings with distinct atomic arrangements usually lead to a marked deviation in the electronic

structures and thus catalytic properties from each other (*8*, *9*, *14*–*16*). For example, the FCC Ru nanostructure exhibits an exceptionally high electrocatalytic activity toward the hydrogen evolution reaction (HER) compared with its HCP counterpart, which originates from a modulation of *d*-band center position and thus the adsorption energies of key intermediates (*14*). Recently, our group reported the epitaxially grown 4H-phase Ru nanostructure that exhibits excellent electrocatalytic performance toward the HER in alkaline media (*17*). Moreover, the FCT FePt nanoparticle, as one kind of non–closest-packed metal nanostructures, has shown superior electrocatalytic activity compared with its closest-packed counterpart (i.e., FCC phase) when it was used for the HER (*18*). Therefore, introduction of a large number of vacancy sites into metallic nanostructures toward a highly voided packing mode, such as those with a vacated Barlow packing (VBP), might exhibit an exciting perspective for electrocatalysis based on their unique defective structures and *d*-band characters. Unfortunately, such nanostructures are energetically unfavorable and very difficult to chemically synthesize. Accordingly, their catalytic application and structure-property relationship remain elusive so far.

Here, we report a facile chemical synthetic method for the preparation of hierarchical Rh nanostructures (Rh NSs), composed of ultrathin HCP Rh nanosheets with a small amount of interstitial carbon in which a series of nanodomains that adopt VBP with ordered vacancies are coherently embedded. Impressively, the obtained Rh NSs exhibit remarkably enhanced electrocatalytic activity and stability toward the HER in alkaline media, as compared with the Rh/C, commercial Pt/C, and most reported electrocatalysts. At current density of $10 \, \mathrm{mA \, cm^{-2}}$, the Rh NSs only require a low overpotential of 37.8 mV, which is much smaller compared with the Rh/C (58.7 mV) and commercial Pt/C (66.0 mV). Moreover, theoretical calculations reveal that the exceptional electrocatalytic performance of Rh NSs toward the HER in alkaline media is mainly attributed to their unique non–close-packed VBP structures.

RESULTS

The Rh NSs were synthesized via a simple one-pot solvothermal method in the presence of rhodium(III) acetylacetonate [Rh(acac)$_3$], oleylamine, oleic acid, and formaldehyde at a reaction time of 14 hours (see the Supplementary Materials and Methods for details). The scanning electron microscopy images show that the as-synthesized Rh NSs have a uniform spherical shape and a jagged surface with size of 218.1 ± 31.3 nm (fig. S1). Transmission electron microscopy (TEM) and high-angle annular dark-field scanning TEM (HAADF-STEM) images taken along two orthogonal directions identify that the synthesized Rh NSs are hierarchically structured and composed of ultrathin nanosheets (Fig. 1, A and B, and fig. S2) with lateral size of 21.4 ± 7.6 nm (fig. S2C) and thickness of 3.7 ± 1.1 nm (fig. S2E). The energy-dispersive x-ray spectroscopy (EDS) confirms that the Rh NSs are almost free of oxygen but contain a small amount of carbon possibly arising from the organic ligands, which excludes the formation of rhodium oxide (fig. S3). In addition, on the basis of measurements by electron spin resonance (fig. S4) and thermogravimetry-differential thermal analysis–mass spectrometry (fig. S5), no rhodium hydride in Rh NSs has been detected. The x-ray absorption spectroscopy and the x-ray photoelectron spectroscopy spectrum of Rh NSs further prove the metallic state of
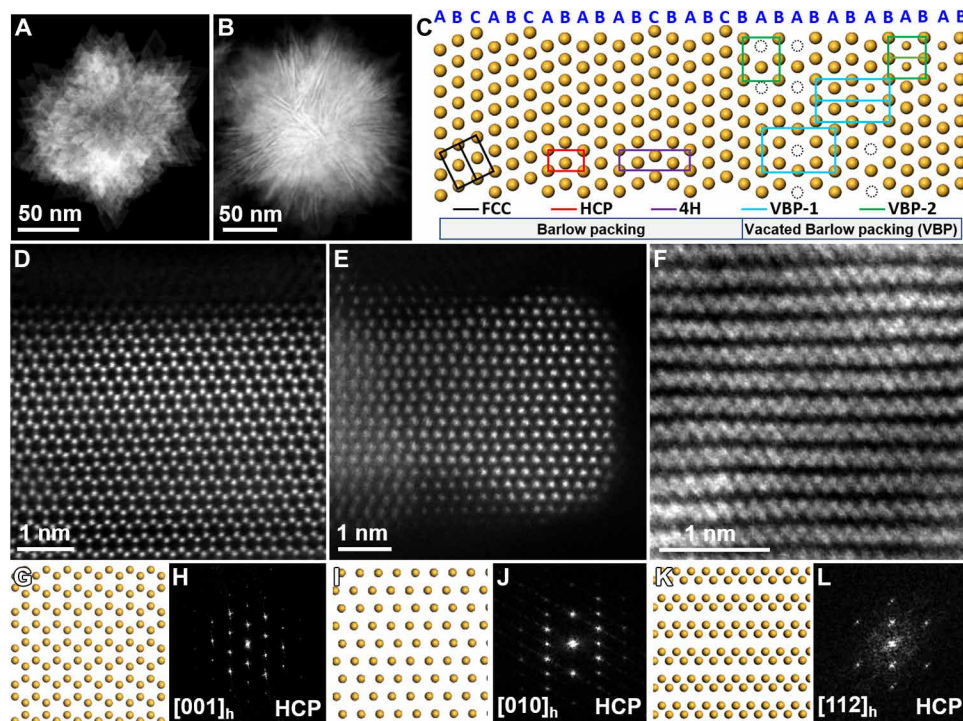
Fig. 1. Morphology and structure characterization of Rh NSs with HCP structure. (**A** and **B**) HAADF-STEM and (**D** to **F**) HRSTEM images of Rh NSs. (C) Projected crystallographic structural models and unit cells of diverse Barlow packings (FCC, HCP, and 4H) and VBPs (VBP-1 and VBP-2) perpendicular to the stacking direction. The black dotted circles represent the Rh vacancies. Regular and small spheres in orange represent the fully and half occupied atomic columns, respectively. Unit cell orientations of VBP-1 and VBP-2 are [010]$_o$ (left) and [011]$_o$ (right). (**G**, **I**, and **K**) Projected crystallographic structural modes and (**H**, **J**, and **L**) FFT patterns: (G and H) in (D) along the [001]$_h$ direction, (I and J) in (E) along the [010]$_h$ direction, and (K and L) in (F) along the [112]$_h$ direction.

Rh (fig. S6). Moreover, the HCP structure of Rh NSs can be directly determined by characterizing the nanostructure along multiple zone axes at atomic resolution using HAADF-STEM (Fig. 1, D to L), where these Z-contrast images (Fig. 1, D to F) closely resemble the structural projections of an HCP Rh, and their fast Fourier transform (FFT) patterns can be well indexed by the HCP cell along its $[001]$, $[010]_h$, and $[112]_h$ directions, respectively (Fig. 1, G to L). As is well known, monometallic nanostructures usually adopt one of those polytypes of Barlow packing modes as the ground-state geometry, where hexagonal atomic sheets are stacked with different sequences as schematically shown in Fig. 1C. It is worth noting that the synthesized Rh NSs have an unusual HCP rather than the conventional FCC structure. In addition, it is observed that the spherical Rh NSs are terminated by the sharp edges of Rh nanosheets (Fig. 1A and fig. S2), which correspond to the $\{010\}_h$ microfacets from the high-resolution STEM (HRSTEM) images (fig. S7).

By further inspecting the HRSTEM images of Rh NSs along the equivalent $[010]_h/[110]_h$ directions of the HCP structure where the stacking order can be explicitly identified (Fig. 2), it is unexpected to observe a large number of nanometer-sized regions with FFT patterns (Fig. 2, H to K) distinct from that of an HCP structure (Fig. 1J). Specifically, four different types of FFT patterns are observed (Fig. 2, H to K), in which additional reflections locate at the simple fractions of the reciprocal vectors, and those representative reflections are marked with indices as (i) $\left(\bar{\tfrac{1}{2}}\,0\,1\right)_h$ (marked by red dotted circle in Fig. 2H) and $\left(\tfrac{1}{2}\,0\,1\right)_h$ (marked by yellow dotted circle in Fig. 2H), (ii) $\left(\tfrac{1}{2}\,0\,0\right)_h$ (marked by yellow dotted circle in Fig. 2I) and $(0\,0\,1)_h$ (marked by red dotted circle in Fig. 2I), (iii) $(0\,0\,1)_h$ (marked by red dotted circle in Fig. 2J), and (iv) $\left(1\,\bar{1}\,\tfrac{1}{2}\right)_h$ (marked by red dotted circle in Fig. 2K). It is well known that HAADF-STEM adopts the Z^2-dependence contrast and is insensitive to the light element. Accordingly, these superstructure reflections originate from the spanning of repeating unit over multiple unit cells and the breaking of $p2gm$ projection symmetry of the HCP structure along $[010]_h/[110]_h$ directions, representing a commensurate modulation of the Rh sublattice. Close inspection of the corresponding regions in the HRSTEM images associated with these FFT patterns allows us to observe a subtle but ordered variation of atomic column intensities from those of an HCP structure (Fig. 2, B and C). The alternating bright and dim contrasts of Rh columns in the region S_1 of Fig. 2B become more apparent by selectively overweighting the weak superstructure spots in the reconstructed STEM image along the $[010]_h/[110]_h$ direction (Fig. 2L), indicating the formation of two types of superstructures with rectangular projection symmetries, which are also confirmed by the FFT patterns in Fig. 2 (H and I). Specifically, one type of these superstructures doubles the periodicity of the HCP lattice along the $[210]_h/[1\bar{1}0]_h$ direction, while the other double periodicities along both $[210]_h/[1\bar{1}0]_h$ and $[001]_h$ directions (i.e., refer to yellow and blue projected unit cells, respectively, in Fig. 2L and fig. S8). A different type of superstructure confirmed by the FFT pattern in Fig. 2J is observed along another equivalent $[010]_h/[110]_h$ projection (Fig. 2C), characterized by the alternating bright and dim rows of Rh columns as marked by red arrows. From the denoised image by real-space averaging (19, 20) over the region S_2 of Fig. 2C (Fig. 2M), there are also nanodomains with doubled periodicity along the $[001]_h$ direction through replacing every other dim rows of Rh columns by bright ones, according to the integrated intensity profiles of Rh rows and FFT pattern (Fig. 2K). It indicates that the observed superstructure arises from an

"occupational modulation" of the Rh sublattice, i.e., nanodomains with ordered Rh vacancies embedded in the Rh NSs. Together, the aforementioned structural projections (Fig. 2, B and C) and the corresponding FFT patterns (Fig. 2, H to K) can be assigned to two polytypes of orthorhombic VBP structures, composed of perfect and vacated $(001)_h$ Rh layers, respectively, with an "ABAB…" stacking sequence. Specifically, they are classified as follows (Fig. 2A): One with half of the Rh columns vacated in every other $(001)_h$ layer of the same type (i.e., either "A" or "B" type) is denoted as VBP-1 (APF = 0.65), and the other with half of the Rh columns vacated in every $(001)_h$ layer of the same type is denoted as VBP-2 (APF = 0.56). These VBP Rh NSs intergrow coherently with the Rh HCP structure but break its hexagonal symmetry (space group: $P6_3/mmc$) to form an orthorhombic structure (Fig. 2A; space group: $Pmm2$) upon an orientation relationship of $\{100\}_o[010]_o//\{001\}_h[010]_h$. As schematically illustrated in Fig. 2 (D to G), the embedded models composed of HCP host matrix and VBP-1/VBP-2 defective nanodomains have distinct projections along the $[010]_h$ and $[110]_h$ directions that are actually symmetry equivalent for the HCP structure (Fig. 1C). The VBP models are further validated by systematically investigating the simulated Z^2-maps and FFT patterns along diverse projections (i.e., $[001]_h$, $[010]_h$, $[110]_h$, $[112]_h$, $[012]_h$, and $[2\bar{1}1]_h$), which qualitatively resemble the experimental HRSTEM images and FFT patterns (Fig. 2 and figs. S7 to S13). Similarly, the effect on image contrast from other local structural features, such as stacking faults and dislocations, is also excluded (figs. S14 to S23). Notably, it is relatively rare to observe VBP nanodomains upon the $[001]_h$ projection, which are actually featured by the uneven contrast of hexagonally arranged atomic columns as indicated by the red arrows in Fig. 2T averaged from region S_4 in Fig. 2R, the presence of $\left(\tfrac{1}{2}\,\tfrac{1}{2}\,0\right)_h$ (marked by red dotted circle in Fig. 2U) and $\left(\bar{\tfrac{1}{2}}\,\tfrac{1}{2}\,0\right)_h$ (marked by yellow dotted circle in Fig. 2U) superstructure reflections in the FFT (Fig. 2U), and short coherence length along the $[210]_h$ direction (Fig. 2, R to T). In contrast, simply tilting the Rh sheet by 17° to the $[112]_h$ direction allows clear identification of VBP nanodomains near the edge of the Rh nanosheet based on the alternating bright and dim contrasts of Rh columns as marked by the red arrows in Fig. 2P averaged from region S_3 in Fig. 2N and the appearance of $\left(1\,0\,\bar{\tfrac{1}{2}}\right)_h$ (marked by red dotted circle in Fig. 2Q) and $\left(0\,1\,\bar{\tfrac{1}{2}}\right)_h$ (marked by yellow dotted circle in Fig. 2Q) superstructure reflections in the FFT (Fig. 2Q). We propose that the short coherence length of VBP nanodomains and frequent domain switching along the $[001]_h$ stacking direction observed in Fig. 2 (B to M) would average out any symmetry-breaking contrast arising from those polytypes of VBP nanodomains that are distributed with the symmetry-equivalent "threefold twin orientations" along the $[001]_h$ direction (fig. S24). Tilting may help bring back the VBP-related contrast near the edge of the Rh nanosheet, which allows the direct visualization of VBP nanodomains with different orientations (fig. S25). Besides the ordered Rh vacancies, it is found that the Rh NSs are further modulated by a small fraction of ordered interstitial carbon atoms in the octahedral voids of the HCP lattice (fig. S26), based on the correlated HAADF- and ABF-STEM imaging results and EDS analysis (figs. S3 and S27). HAADF-STEM can only probe the Rh sublattice and superstructures arising from the ordered Rh vacancies rather than the light interstitial atoms (figs. S26C and fig. S27, A to D), while ABF-STEM can probe the interstitial light elements to discriminate between perfect HCP and superstructures mainly arising from interstitial carbon atoms [figs. S26D, S27 (E to H), S28, and S29].
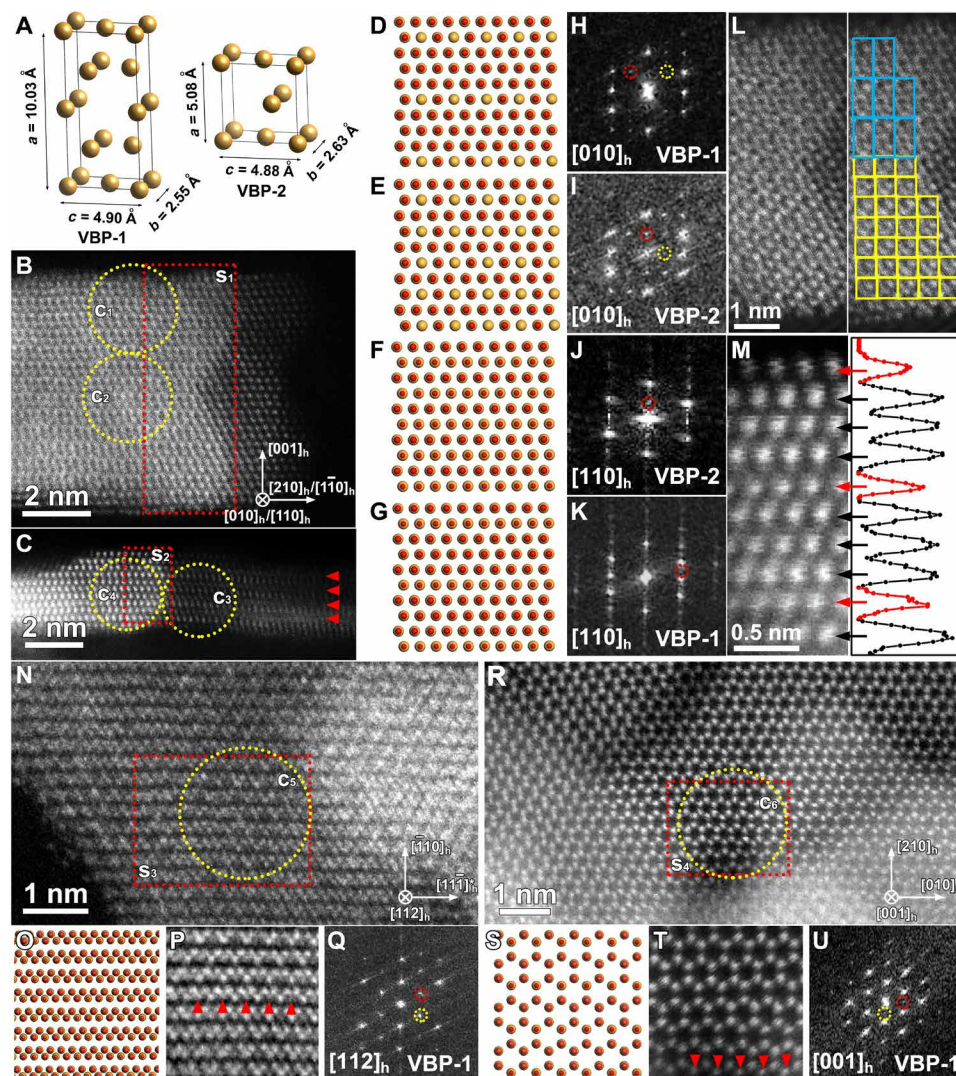
Fig. 2. HRSTEM images and structural elucidation of Rh NSs with VBP nanodomains. (**A**) Schematic illustration of the unit cells for VBP-1 and VBP-2 structures. Unit cell parameters are extracted from the HRSTEM images. (**B** and **C**) HRSTEM images of Rh NSs taken along the $[010]_h/[110]_h$ directions. Red arrowheads refer to the row of Rh columns with dim contrast. (**D** to **G**) Projected supercell models with superimposed HCP (spheres in orange) and VBP (regular and small spheres in red representing the fully and half-occupied atomic columns, respectively) structures, and (**H** to **K**) FFT patterns taken from regions in yellow dotted circles C_1 to C_4 in (B) and (C). (**L**) Reconstructed HRSTEM image from region S_1 in (B) through overweighting the superstructure reflections by a factor of six. Blue and yellow rectangles refer to the projected unit cells for VBP-1/VBP-2 phases. (**M**) The real-space averaged images over the region S_2 in (C) and the corresponding integrated intensity profiles of atomic rows marked by black (bright) and (dim) red arrows. (**N** and **R**) HRSTEM images, (**O** and **S**) projected supercell models, (**P** and **T**) the real-space averaged images over regions S_3 and S_4, and (**Q** and **U**) FFT patterns from circle C_5 and C_6 in images (N, R) of Rh NSs along the $[112]_h$ and $[001]_h$ directions, respectively.

Therefore, on the basis of the reconstructed HAADF- and ABF-STEM images taken along the $[010]_h/[110]_h$ direction with overweighted superstructure modulations, it is observed that the Rh vacancies are short range correlated with periods spanning a few nanometers, while the octahedral voids of the HCP Rh lattice are partially filled by interstitial carbon with long-range order (fig. S27). As quantified by x-ray diffraction (XRD) and Rietveld whole-pattern fitting (fig. S30), merely about one of eight octahedral voids is occupied by the interstitial carbon. However, the nanoscopically ordered VBP structures can only be observed by the electron microscopy (Fig. 2) with negligible contribution to XRD patterns (fig. S31). On the basis of the aforementioned results, the Rh NSs with the coexistence of short-range ordered Rh vacancies (i.e., VBP domains), long-range ordered monometallic Rh, and a small amount of the

interstitial carbon have been prepared, which further assemble into spherical particles.

To study the formation mechanism of Rh NSs, time-dependent experiments were conducted (figs. S32 and S33). It was found by STEM imaging that the product obtained at reaction time of 1 hour adopted an HCP structure (fig. S34), and the VBP structures appeared at reaction time of 3 hours (fig. S35). The hierarchical structures composed of ultrathin Rh nanosheets endow the Rh NSs, the final product at reaction time of 14 hours, with unique capability of embedding nanostructures with ordered vacancies, arising from the oriented attachment of these $(001)_h$-oriented nanosheets both laterally and vertically (fig. S7 and Fig. 2, B and C), forming chemically bonded and coherent interfaces. The oriented attachment of nanosheets in a staggered manner will also create abundant notch

sites near the edges with very small intersheet spacings down to atomic thickness, as schematically shown in fig. S7C. Unlike the intercalation of hetero-components into van der Waals stacked two-dimensional layered materials with highly flexible interlayer spacings (21–23), the intercalation of Rh atoms into these notch sites formed by chemically bonded and rigidly stacked Rh nanosheets is however restricted by the extremely slow diffusion kinetics of Rh adatoms, resulting in the formation of thermodynamically unfavorable VBP structures. Accordingly, the VBP nanodomains preferentially grow at the junctions of multiple Rh nanosheets as identified from both the top view (fig. S7) and side view (Fig. 2B and fig. S36) of the nanosheets. This phenomenon is more pronounced from a tilted side view of the nanosheets (Fig. 2C and fig. S36), where VBP nanodomains at the junction of nanosheets are composed of the partially intercalated notch sites (as indicated by the red arrows) that are formed by the oriented attachment of Rh nanosheets with a single-atom thickness. These intercalated notch sites then become $(001)_h$ atomic layers with ordered Rh vacancies and create superstructures with modulated STEM contrast. By calculating the size-dependent formation energy of VBP nanodomains embedded in the HCP structure (Fig. 1C and table S1), it is found that the HCP structure plays an essential role stabilizing the VBP nanodomains, especially those with smaller size. Actually, the Rh VBP/HCP hetero-phase structure is thermally stable up to ~200°C in Ar and can completely transform into an FCC structure at 350°C with disordered intermediate as observed by XRD (fig. S37). It indicates that the VBP/HCP-FCC phase transformation might follow a "reconstructive" reordering mechanism, which is mediated by a disordered polytypic intermediate (24), rather than the Shockley partial dislocation gliding mechanism as usually proposed in the HCP-FCC phase transformation (24).

Previous studies have demonstrated that noble metal nanomaterials with unusual crystal structures (9, 14, 17, 18, 25–28) and defects (5, 29–35) exhibit promising catalytic applications. As a proof-of-concept application, the electrocatalytic HER performance of Rh NSs with the optimum Rh loading was evaluated in alkaline media (fig. S38). For comparison, the commercial Pt/C [20 weight % (wt %) Pt on Vulcan XC-72R carbon; fig. S39] and Rh/C (see the Supplementary Materials for preparation details; fig. S40) were used as reference catalysts. Figure 3A shows the representative polarization curves of Rh NSs, Rh/C, and Pt/C recorded at a scan rate of 5 mV s^{-1} in 1.0 M KOH aqueous solution (with ohmic drop correction). It is obvious that the Rh NSs exhibit much higher HER activity as compared with the Rh/C and Pt/C. Specifically, at potential of −70 mV [versus reversible hydrogen electrode (vs. RHE)], the current density of Rh NSs reaches 21.7 mA cm^{-2}, which is about 1.8 and 2.0 times those of Rh/C (12.4 mA cm^{-2}) and Pt/C (10.9 mA cm^{-2}), respectively. Moreover, at current density of 10 mA cm^{-2}, the Rh NSs require a low overpotential of 37.8 mV, much lower than those of Rh/C (58.7 mV) and Pt/C (66.0 mV) (Fig. 3B, left; fig. S41; and table S2). It is worth mentioning that the overpotential, 37.8 mV, is comparable to or even smaller than those of the reported advanced electrocatalysts (Fig. 3C and table S3).

To gain more insight into the kinetics of HER, further analysis of the Tafel slope was performed (36). As shown in Fig. 3D and fig. S42,
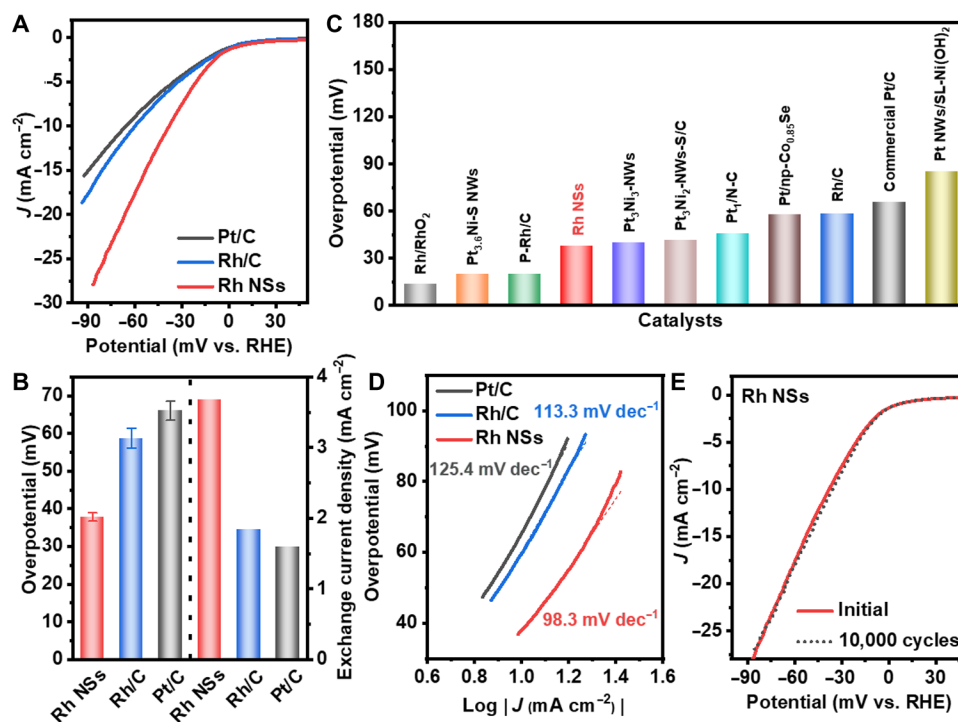
Fig. 3. HER activity and stability of Rh NSs, Rh/C, and Pt/C. (**A**) Polarization curves of Rh NSs, Rh/C, and commercial Pt/C. Linear sweep voltammetry was carried out in 1.0 M KOH aqueous solution at scan rate of 5.0 mV s^{-1}. (**B**) Overpotentials at current density of 10 mA cm^{-2} (left) and exchange current densities (right) of Rh NSs, Rh/C, and commercial Pt/C. The error bars were obtained on the basis of the measurements of five samples. (**C**) Comparison of the overpotentials of Rh NSs, Rh/C, commercial Pt/C, and previously reported electrocatalysts at current density of 10 mA cm^{-2} in 1.0 M KOH aqueous solution. (**D**) Tafel plots obtained from the corresponding polarization curves of Rh NSs, Rh/C, and commercial Pt/C. (**E**) Durability test of Rh NSs. The polarization curves were recorded before and after 10,000 potential cycles in 1.0 M KOH aqueous solution from 0.1 to −0.1 V (vs. RHE).

at both low- and high-overpotential regions, the Rh NSs display much smaller Tafel slopes compared with Rh/C and Pt/C, indicating more efficient HER kinetics of Rh NSs (30,37). Theoretical calculations further imply that the Volmer step is rate determining (fig. S43). Using the Butler-Volmer fitting (figs. S42 and S44) (38–40), the exchange current densities were determined (Fig. 3B, right). Obviously, the Rh NSs achieve the greatest value of 3.68 mA cm^{-2} compared with Rh/C (1.84 mA cm^{-2}) and Pt/C (1.59 mA cm^{-2}), confirming the superior intrinsic HER activity of Rh NSs. By using the Cu underpotential deposition method (fig. S45) (14, 41–43), the electrochemical active surface area (ECSA) of Rh NSs was measured to be 48.7 m^2 g^{-1}, which is smaller than that of Pt/C (63.7 m^2 g^{-1}) but much greater than that of Rh/C (32.3 m^2 g^{-1}) (table S4). The aforementioned ECSA values are consistent with those obtained from CO stripping (fig. S46 and table S5). At overpotential of 50 mV, Rh NSs exhibit a turnover frequency of 4.05 H$_2$ s^{-1}, remarkably greater than those of Pt/C (1.61 H$_2$ s^{-1}), Rh/C (3.51 H$_2$ s^{-1}), and some reported HER electrocatalysts (tables S3 and S4 and fig. S47). In Fig. 3E, no obvious shift in the HER polarization curves was observed before and after 10,000 potential cycles. In addition, the structure of Rh NSs after the durability test was further characterized by TEM (fig. S48), showing negligible changes in the shape, size, and phase. The I-t curves of Rh NSs at different current densities in 1.0 M KOH aqueous solution were measured, further confirming the good stability of Rh NSs (fig. S49). Moreover, the long-term (240 hours) HER test was conducted at high current density of 1.5 A cm^{-2}. As shown in fig. S50A, no obvious change in the overpotential was observed during the test. In addition, the polarization curves were also recorded before and after the test, showing the negligible shift (fig. S50B). The aforementioned results suggest that the Rh NSs are highly active and stable for the electrocatalytic HER in alkaline media.

DISCUSSION

To understand the exceptional HER performance of Rh NSs with VBP nanodomains in alkaline media, the density functional theory (DFT) calculations were performed. As shown in fig. S51, the H adsorption on various Rh surfaces was first studied. H adsorption on Pt surface was used as the reference of catalyst for HER (44, 45). It shows that the adsorption energies of H on all Rh surfaces are more negative than that on Pt surface (Fig. 4A and table S6). Particularly, the adsorption energy of H on the VBP-1 Rh(010) surface is almost equal to that of the Pt(111) surface (−0.452 eV versus −0.441 eV) (table S6), implying an optimum adsorption behavior of H on the VBP-1 Rh(010) surface toward HER. On the basis of the Volmer reaction in alkaline solution, the adsorption of H$_2$O and the dissociation of H$_2$O should be taken into account (14, 41, 46). In general, a more negative adsorption energy of H$_2$O, meaning the stronger adsorption of H$_2$O, is preferred for HER in alkaline media since it can accelerate the Volmer reaction (41, 46). As shown in Fig. 4A, fig. S52, and table S6, the VBP-1 Rh(001) and VBP-1 Rh(010) surfaces exhibit more negative adsorption energies of H$_2$O, i.e., −0.720 and −0.514 eV, respectively, which are significantly more negative than that on Pt(111) surface (−0.215 eV). The dissociation reactions of H$_2$O on various surfaces are shown in fig. S53. Consistent with previous reports (14, 41, 46, 47), Pt(111) displays a high H$_2$O dissociation energy of 0.690 eV (table S7), indicating that it is inefficient for H$_2$O dissociation. In sharp contrast, VBP-1 Rh(010) and VBP-1 Rh(001) show the remarkably reduced H$_2$O dissociation energies of 0.040 and −0.589 eV, respectively (table S7). This indicates that both VBP-1 Rh(010) and VBP-1 Rh(001) are more efficient for cleaving the O—H bond in H$_2$O, indicating good HER performance in alkaline solution than does Pt(111).

The VBP-1 Rh(010) surface has suitable adsorption and dissociation energies, arising from the unique VBP structure with Rh vacancies on the surface (Fig. 2). From the configurations of HCP Rh (010) surfaces, it is found that H prefers to stay at "hollow" site (center of three adjacent atoms, but different from a close packed surface), and H$_2$O prefers to stay at top site (figs. S51 and S52). An Rh vacancy in VBP-1 Rh(010) breaks the hollow site (Fig. 4B), resulting in relatively more positive adsorption energies for H. Therefore, the adsorption energy of H on the VBP-1 Rh(010) surface becomes closer to that of the Pt(111) surface, which is favorable for the HER. However, in case of H$_2$O adsorption, the Rh vacancy makes the adjacent Rh atoms more active (Fig. 4C), which leads to the enhanced adsorption
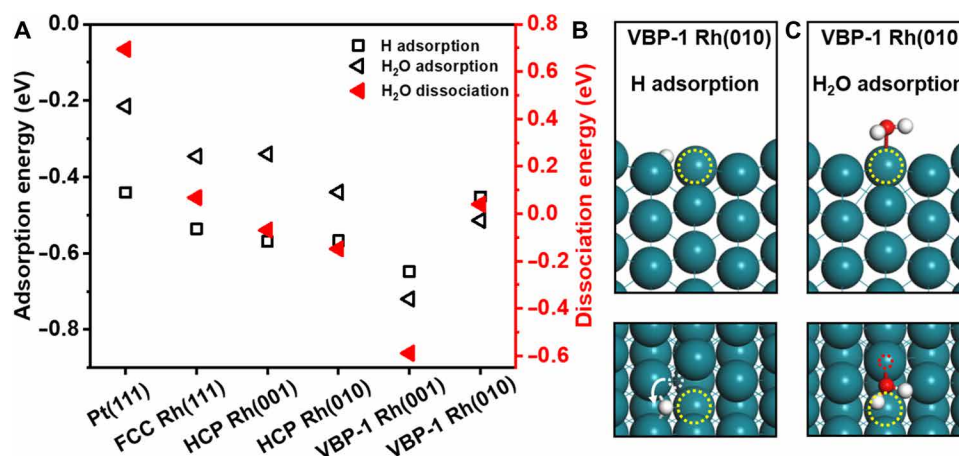
Fig. 4. Adsorption of H and H$_2$O, dissociation of H$_2$O, and HER reactions on various Rh surfaces and Pt(111) surface. (**A**) Adsorption energies of H and H$_2$O on Pt(111), FCC Rh(111), HCP Rh(001), HCP Rh(010), VBP-1 Rh(001), and VBP-1 Rh(010) surfaces (left, black), and the dissociation energies of H$_2$O on these surfaces (right, red). (**B** and **C**) Side and top views of H and H$_2$O adsorbed on VBP-1 Rh(010) surfaces. The yellow dotted circles mark the removed Rh atoms. The white and red dotted circles mark the best adsorption sites before the Rh atoms are removed.

of H_2O molecules. Together, it is concluded that the excellent electrocatalytic performance of Rh NSs toward HER in alkaline media mainly originates from the VBP structures, which facilitate the adsorption and dissociation of H_2O.

In summary, we report a chemical synthesis of energetically highlying metallic Rh NSs with ordered vacancies, which are coherently embedded and stabilized by a densest-packed HCP Rh structure. These highly voided metallic nanostructures have polytypes that adopt diverse VBPs and orthorhombic symmetry, which comprise perfect and vacated nanosheets with distinct stacking sequences. The production of these thermodynamically unfavorable vacated nanostructures could be closely related with the unique hierarchical structure of Rh NSs assembled and chemically bonded by ultrathin Rh nanosheets, which could create atom-wide notch sites that allow the slow and incomplete intercalation of Rh atoms toward the formation of VBP nanostructures. These metastable VBP metallic nanostructures outperform most reported and commercial electrocatalysts toward the HER in alkaline media, which arises from the greatly facilitated adsorption and dissociation of H_2O molecules in the HER by the vacancy structures based on theoretical calculations. This work may pave the way toward the vacancy engineering of nanomaterials with unique physicochemical properties and various promising applications.

MATERIALS AND METHODS
Reagents
Rh(acac)$_3$ (97%), oleylamine (≥98%), oleic acid (90%), formaldehyde solution (37%), potassium hydroxide (KOH, ≥85%), and other chemicals used in the experiments without special mention were all purchased from Sigma-Aldrich. Ethanol (absolute, 99.9%) and *n*-hexane were purchased from Merck (Nordic European Centre, Singapore). Nafion alcohol solution (5 wt %) was purchased from Alfa Aesar. The Milli-Q water was obtained from the Milli-Q System. All the materials were used as received without further purification.

Methods
Synthesis of hierarchical Rh NSs composed of ultrathin nanosheets
In a typical procedure for the synthesis of Rh NSs, Rh(acac)$_3$ (8 mg) was added into a 23.0-ml Teflon-lined stainless steel autoclave containing oleylamine (9.0 ml) and oleic acid (1.0 ml). After the mixture underwent magnetic stirring for 10 min, sonication for 10 min, and subsequent magnetic stirring for 5 min, formaldehyde solution (0.8 ml) was added under magnetic stirring. The obtained mixture was continuously stirred for 15 min at room temperature. Then, the Teflon-lined stainless steel autoclave was sealed and heated from room temperature to 170°C at a heating rate of 2°C min^{-1}. After being maintained at 170°C for 14 hours, it was cooled down to room temperature naturally. Last, after the resulting product, i.e., Rh NSs, was collected by centrifugation at 9000 rpm for 5 min and washed five times with *n*-hexane and then ethanol, it was dispersed in ethanol for further characterization.

Synthesis of Rh/C catalysts
The Rh/C catalysts were prepared using the previously reported method (*14*). Typically, 10 ml of RhCl$_3$ aqueous solution (19.4 mM) and the Vulcan XC-72R carbon (100 mg) dispersed in 10 ml of ethanol were mixed and sonicated for 1 hour. After that, the mixture

was concentrated using a rotary evaporator and then completely dried using a freeze dryer. Last, the as-obtained black powder was annealed under Ar atmosphere at 600°C for 1 hour at a heating rate of 2°C min^{-1}.

Electrochemical measurements
All electrochemical measurements were conducted using a standard three-electrode cell system on an Autolab electrochemical workstation (PGSTAT12) at room temperature (~25°C). A glassy carbon electrode (GCE) with diameter of 3 mm coated with catalysts was used as working electrode. The Hg/HgO and graphite rod were used as reference electrode and counter electrode, respectively. Before the electrochemical test, the GCE was successively polished with 300- and then 50-nm Al$_2$O$_3$ slurry. After it was washed with Milli-Q water and ethanol to obtain a clean surface and dried in air, 3.0 µl of catalyst solution containing Rh NSs (0.401 mg ml^{-1} Rh measured by inductively coupled plasma optical emission spectrometry) was dropped onto its surface to achieve the Rh loading of 0.017 mg cm^{-2}. After being dried in air for 2 hours, the prepared GCE coated with Rh NSs was irradiated under an ultraviolet lamp (10 W with emission of 185 and 254 nm) for 4 hours, which was placed ~5 mm away from the GCE, to remove the capping agent on Rh NSs (*48–50*). Last, 2 µl of Nafion ethanolic solution (0.1 wt %) was dropped onto the electrode surface. After being dried in air for 2 hours, the electrode was used as the working electrode for the electrochemical measurement.

The commercial Pt/C catalyst was prepared by the aforementioned method. The loading amount of Pt in Pt/C was the same as that of Rh NSs. The electrocatalytic hydrogen evolution activities of the catalysts were evaluated by the linear sweep voltammetry in 1.0 M KOH aqueous solution at scan rate of 5.0 mV s^{-1}. The accelerated durability tests were performed at room temperature in 1.0 M KOH aqueous solution by applying the cyclic potential sweeps between 0.1 and −0.1 V (vs. RHE) at scan rate of 100 mV s^{-1} for 10,000 cycles. Electrochemical impedance spectroscopy was measured from 100 kHz to 0.1 Hz to obtain the solution resistance (R_s), and all data were corrected with R_s (fig. S54).

According to the previously reported method (*38–40*, *51*, *52*), the exchange current density (J_0) is determined by fitting the kinetic current density (J_k) with the Butler-Volmer equation

$$J_k = J_0 \left[e^{\left(\frac{\alpha F}{RT}\right)\eta} - e^{\left[\frac{-(1-\alpha)F}{RT}\right]\eta} \right]$$

where α represents the transfer coefficient, η indicates the overpotential, F is Faraday constant (96,485 C mol^{-1}), R is the universal gas constant (8.314 J mol^{-1} K^{-1}), and T is the temperature in Kelvin (298 K). The kinetic current density can be calculated by using the Koutecky-Levich equation as follows

$$\frac{1}{J} = \frac{1}{J_k} + \frac{1}{J_d}$$

where J is the solution resistance (iR)–corrected current density measured in an H$_2$-saturated 1.0 M KOH solution at a sweep rate of 5 mV s^{-1}, and J_d is the diffusion limited current density.

In the electrochemical measurements, the Hg/HgO reference electrode was calibrated with respect to the RHE by testing cyclic voltammogram in a highly pure H$_2$-saturated 1.0 M KOH aqueous solution using Pt wires as working electrode and counter electrode. The value of the potential at current density of zero was regarded as the thermodynamic potential for the electrocatalytic HER (fig. S55).

Therefore, the potential with respect to RHE in our measurements can be calculated according to the following equation (*53*)

$$E(\text{RHE}) = E(\text{Hg/HgO}) + 0.950\ \text{V}$$

SUPPLEMENTARY MATERIALS

Supplementary material for this article is available at http://advances.sciencemag.org/cgi/content/full/7/13/eabd6647/DC1

REFERENCES AND NOTES

1. M. Setvin, M. Wagner, M. Schmid, G. S. Parkinson, U. Diebold, Surface point defects on bulk oxides: Atomically-resolved scanning probe microscopy. *Chem. Soc. Rev.* **46**, 1772–1784 (2017).
2. Z. Sun, K. Ikemoto, T. M. Fukunaga, T. Koretsune, R. Arita, S. Sato, H. Isobe, Finite phenine nanotubes with periodic vacancy defects. *Science* **363**, 151–155 (2019).
3. J. Jia, C. Qian, Y. Dong, Y. F. Li, H. Wang, M. Ghoussoub, K. T. Butler, A. Walsh, G. A. Ozin, Heterogeneous catalytic hydrogenation of CO_2 by metal oxides: Defect engineering – perfecting imperfection. *Chem. Soc. Rev.* **46**, 4631–4644 (2017).
4. H.-S. Kim, J. B. Cook, H. Lin, J. S. Ko, S. H. Tolbert, V. Ozolins, B. Dunn, Oxygen vacancies enhance pseudocapacitive charge storage properties of MoO_{3-x}. *Nat. Mater.* **16**, 454–460 (2017).
5. Y. Wang, P. Han, X. Lv, L. Zhang, G. Zheng, Defect and interface engineering for aqueous electrocatalytic CO_2 reduction. *Joule* **2**, 2551–2582 (2018).
6. T. C. Hales, A proof of the Kepler conjecture. *Ann. Math.* **162**, 1065–1185 (2005).
7. Y. Chen, Z. Lai, X. Zhang, Z. Fan, Q. He, C. Tan, H. Zhang, Phase engineering of nanomaterials. *Nat. Rev. Chem.* **4**, 243–256 (2020).
8. H. Cheng, N. Yang, Q. Lu, Z. Zhang, H. Zhang, Syntheses and properties of metal nanomaterials with novel crystal phases. *Adv. Mater.* **30**, 1707189 (2018).
9. Z. Fan, H. Zhang, Crystal phase-controlled synthesis, properties and applications of noble metal nanomaterials. *Chem. Soc. Rev.* **45**, 63–82 (2016).
10. K. Kusada, H. Kitagawa, A route for phase control in metal nanoparticles: A potential strategy to create advanced materials. *Adv. Mater.* **28**, 1129–1142 (2016).
11. I. Kovacs, H. E. Sayed, Point defects in metals. *J. Mater. Sci.* **11**, 529–559 (1976).
12. C. M. Sánchez-Sánchez, J. Solla-Gullón, F. J. Vidal-Iglesias, A. Aldaz, V. Montiel, E. Herrero, Imaging structure sensitive catalysis on different shape-controlled platinum nanoparticles. *J. Am. Chem. Soc.* **132**, 5622–5624 (2010).
13. M. T. M. Koper, Structure sensitivity and nanoscale effects in electrocatalysis. *Nanoscale* **3**, 2054–2073 (2011).
14. Y. Zheng, Y. Jiao, Y. Zhu, L. H. Li, Y. Han, Y. Chen, M. Jaroniec, S. Z. Qiao, High electrocatalytic hydrogen evolution activity of an anomalous ruthenium catalyst. *J. Am. Chem. Soc.* **138**, 16174–16181 (2016).
15. Z. Cao, Q. Chen, J. Zhang, H. Li, Y. Jiang, S. Shen, G. Fu, B. A. Lu, Z. Xie, L. Zheng, Platinum-nickel alloy excavated nano-multipods with hexagonal close-packed structure and superior activity towards hydrogen evolution reaction. *Nat. Commun.* **8**, 15131 (2017).
16. J. L. Huang, Z. Li, H. H. Duan, Z. Y. Cheng, Y. D. Li, J. Zhu, R. Yu, Formation of hexagonal-close packed (HCP) rhodium as a size effect. *J. Am. Chem. Soc.* **139**, 575–578 (2017).
17. Q. Lu, A. L. Wang, Y. Gong, W. Hao, H. Cheng, J. Chen, B. Li, N. Yang, W. Niu, J. Wang, Y. Yu, X. Zhang, Y. Chen, Z. Fan, X. J. Wu, J. Chen, J. Luo, S. Li, L. Gu, H. Zhang, Crystal phase-based epitaxial growth of hybrid noble metal nanostructures on 4H/fcc Au nanowires. *Nat. Chem.* **10**, 456–461 (2018).
18. Q. Li, L. Wu, G. Wu, D. Su, H. Lv, S. Zhang, W. Zhu, A. Casimir, H. Zhu, A. Mendoza-Garcia, S. Sun, New approach to fully ordered fct-FePt nanoparticles for much enhanced electrocatalysis in acid. *Nano Lett.* **15**, 2468–2473 (2015).
19. Y. Zhu, J. Ciston, B. Zheng, X. Miao, C. Czarnik, Y. Pan, R. Sougrat, Z. Lai, C. E. Hsiung, K. Yao, I. Pinnau, M. Pan, Y. Han, Unravelling surface and interfacial structures of a metal–organic framework by transmission electron microscopy. *Nat. Mater.* **16**, 532–536 (2017).
20. D. Zhang, Y. Zhu, L. Liu, X. Ying, C. E. Hsiung, R. Sougrat, K. Li, Y. Han, Atomic-resolution transmission electron microscopy of electron beam–sensitive crystalline materials. *Science* **359**, 675–679 (2018).
21. K. S. Novoselov, A. Mishchenko, A. Carvalho, A. H. C. Neto, 2D materials and van der Waals heterostructures. *Science* **353**, aac9439 (2016).
22. C. Wang, Q. He, U. Halim, Y. Liu, E. Zhu, Z. Lin, H. Xiao, X. Duan, Z. Feng, R. Cheng, N. O. Weiss, G. Ye, Y. C. Huang, H. Wu, H. C. Cheng, I. Shakir, L. Liao, X. Chen, W. A. Goddard III, Y. Huang, X. Duan, Monolayer atomic crystal molecular superlattices. *Nature* **555**, 231–236 (2018).
23. Y. Liu, N. O. Weiss, X. Duan, H. C. Cheng, Y. Huang, X. Duan, Van der Waals heterostructures and devices. *Nat. Rev. Mater.* **1**, 16042 (2016).
24. P. Tolédano, G. Krexner, M. Prem, H.-P. Weber, V. P. Dmitriev, Theory of the martensitic transformation in cobalt. *Phys. Rev. B* **64**, 144104 (2001).
25. W.-Z. Li, J. X. Liu, J. Gu, W. Zhou, S. Y. Yao, R. Si, Y. Guo, H. Y. Su, C. H. Yan, W. X. Li, Y. W. Zhang, D. Ma, Chemical insights into the design and development of face-centered cubic ruthenium catalysts for Fischer–Tropsch synthesis. *J. Am. Chem. Soc.* **139**, 2267–2276 (2017).
26. H. Ye, Q. Wang, M. Catalano, N. Lu, J. Vermeylen, M. J. Kim, Y. Liu, Y. Sun, X. Xia, Ru nanoframes with an fcc structure and enhanced catalytic properties. *Nano Lett.* **16**, 2812–2817 (2016).
27. K. Kusada, H. Kobayashi, T. Yamamoto, S. Matsumura, N. Sumi, K. Sato, K. Nagaoka, Y. Kubota, H. Kitagawa, Discovery of face-centered-cubic ruthenium nanoparticles: Facile size-controlled synthesis using the chemical reduction method. *J. Am. Chem. Soc.* **135**, 5493–5496 (2013).
28. Q. Zhang, K. Kusada, D. Wu, T. Yamamoto, T. Toriyama, S. Matsumura, S. Kawaguchi, Y. Kubota, H. Kitagawa, Selective control of fcc and hcp crystal structures in Au–Ru solid-solution alloy nanoparticles. *Nat. Commun.* **9**, 510 (2018).
29. S. Xie, Q. Xu, X. Huang, Defect-rich metal nanocrystals in catalysis. *ChemCatChem* **8**, 480–485 (2016).
30. C. Li, Q. Yuan, B. Ni, T. He, S. Zhang, Y. Long, L. Gu, X. Wang, Dendritic defect-rich palladium–copper–cobalt nanoalloys as robust multifunctional non-platinum electrocatalysts for fuel cells. *Nat. Commun.* **9**, 3702 (2018).
31. H. Zhang, X. Xia, W. Li, J. Zeng, Y. Dai, D. Yang, Y. Xia, Facile synthesis of five-fold twinned, starfish-like rhodium nanocrystals by eliminating oxidative etching with a chloride-free precursor. *Angew. Chem. Int. Ed.* **49**, 5296–5300 (2010).
32. H. Wang, S. Zhou, K. D. Gilroy, Z. Cai, Y. Xia, Icosahedral nanocrystals of noble metals: Synthesis and applications. *Nano Today* **15**, 121–144 (2017).
33. S. Xie, H. Zhang, N. Lu, M. Jin, J. Wang, M. J. Kim, Z. Xie, Y. Xia, Synthesis of rhodium concave tetrahedrons by collectively manipulating the reduction kinetics, facet-selective capping, and surface diffusion. *Nano Lett.* **13**, 6262–6268 (2013).
34. H. Zhang, W. Li, M. Jin, J. Zeng, T. Yu, D. Yang, Y. Xia, Controlling the morphology of rhodium nanocrystals by manipulating the growth kinetics with a syringe pump. *Nano Lett.* **11**, 898–903 (2011).
35. C.-S. Kuo, C. R. Kao, W. J. Chen, M. Y. Lu, D. A. Cullen, B. T. Sneed, Y. C. Chuang, C. C. Yu, C. H. Kuo, Aqueous synthesis of concave Rh nanotetrahedra with defect-rich surfaces: Insights into growth-, defect-, and plasmon-enhanced catalytic energy conversion. *Chem. Mater.* **30**, 4448–4458 (2018).
36. T. Shinagawa, A. T. Garcia-Esparza, K. Takanabe, Insight on Tafel slopes from a microkinetic analysis of aqueous electrocatalysis for energy conversion. *Sci. Rep.* **5**, 13801 (2015).
37. Z. Zhang, G. Liu, X. Cui, B. Chen, Y. Zhu, Y. Gong, F. Saleem, S. Xi, Y. du, A. Borgna, Z. Lai, Q. Zhang, B. Li, Y. Zong, Y. Han, L. Gu, H. Zhang, Crystal phase and architecture engineering of lotus-thalamus-shaped Pt-Ni anisotropic superstructures for highly efficient electrochemical hydrogen evolution. *Adv. Mater.* **30**, 1801741 (2018).
38. W. Sheng, H. A. Gasteiger, Y. Shao-Horn, Hydrogen oxidation and evolution reaction kinetics on platinum: Acid vs alkaline electrolytes. *J. Electrochem. Soc.* **157**, B1529–B1536 (2010).
39. J. Zheng, W. Sheng, Z. Zhuang, B. Xu, Y. Yan, Universal dependence of hydrogen oxidation and evolution reaction activity of platinum-group metals on pH and hydrogen binding energy. *Sci. Adv.* **2**, e1501602 (2016).
40. W. Sheng, M. Myint, J. G. Chen, Y. Yan, Correlating the hydrogen evolution reaction activity in alkaline electrolytes with the hydrogen binding energy on monometallic surfaces. *Energ. Environ. Sci.* **6**, 1509–1512 (2013).
41. J. Mahmood, F. Li, S. M. Jung, M. S. Okyay, I. Ahmad, S. J. Kim, N. Park, H. Y. Jeong, J. B. Baek, An efficient and pH-universal ruthenium-based catalyst for the hydrogen evolution reaction. *Nat. Nanotechnol.* **12**, 441–446 (2017).
42. C. L. Green, A. Kucernak, Determination of the platinum and ruthenium surface areas in platinum–ruthenium alloy electrocatalysts by underpotential deposition of copper. I. Unsupported catalysts. *J. Phys. Chem. B* **106**, 1036–1047 (2002).
43. L. Colmenares, Z. Jusys, R. J. Behm, Electrochemical surface characterization and O_2 reduction kinetics of Se surface-modified Ru nanoparticle-based $RuSe_y/C$ catalysts. *Langmuir* **22**, 10437–10445 (2006).
44. F. Thomas, K. P. Jorgensen, J. Bonde, J. H. Nielsen, S. Horch, I. Chorkendorff, Identification of active edge sites for electrochemical H_2 evolution from MoS_2 nanocatalysts. *Science* **317**, 100–102 (2007).
45. Z. W. Seh, J. Kibsgaard, C. F. Dickens, I. Chorkendorff, J. K. Nørskov, T. F. Jaramillo, Combining theory and experiment in electrocatalysis: Insights into materials design. *Science* **355**, eaad4998 (2017).
46. R. Subbaraman, D. Tripkovic, D. Strmcnik, K. C. Chang, M. Uchimura, A. P. Paulikas, V. Stamenkovic, N. M. Markovic, Enhancing hydrogen evolution activity in water splitting by tailoring Li^+-$Ni(OH)_2$-Pt interfaces. *Science* **334**, 1256–1260 (2011).

47. N. Danilovic, R. Subbaraman, D. Strmcnik, K. C. Chang, A. P. Paulikas, V. R. Stamenkovic, N. M. Markovic, Enhancing the alkaline hydrogen evolution reaction activity through the bifunctionality of Ni(OH)$_2$/metal catalysts. *Angew. Chem. Int. Ed.* **51**, 12495–12498 (2012).

48. V. Mazumder, S. Sun, Oleylamine-mediated synthesis of Pd nanoparticles for catalytic formic acid oxidation. *J. Am. Chem. Soc.* **131**, 4588–4589 (2009).

49. C. Aliaga, J. Y. Park, Y. Yamada, H. S. Lee, C. K. Tsung, P. Yang, G. A. Somorjai, Sum frequency generation and catalytic reaction studies of the removal of organic capping agents from Pt nanoparticles by UV–ozone treatment. *J. Phys. Chem. C* **113**, 6150–6155 (2009).

50. D. Li, C. Wang, D. Tripkovic, S. Sun, N. M. Markovic, V. R. Stamenkovic, Surfactant removal for colloidal nanoparticles from solution synthesis: The effect on catalytic performance. *ACS Catal.* **2**, 1358–1362 (2012).

51. J. Zheng, Y. Yan, B. Xu, Correcting the hydrogen diffusion limitation in rotating disk electrode measurements of hydrogen evolution reaction kinetics. *J. Electrochem. Soc.* **162**, F1470–F1481 (2015).

52. J. Durst, A. Siebel, C. Simon, F. Hasché, J. Herranz, H. A. Gasteiger, New insights into the electrochemical hydrogen oxidation and evolution reaction mechanism. *Energ. Environ. Sci.* **7**, 2255–2260 (2014).

53. Y. J. Sa, C. Park, H. Y. Jeong, S. H. Park, Z. Lee, K. T. Kim, G. G. Park, S. H. Joo, Carbon nanotubes/heteroatom-doped carbon core–sheath nanostructures as highly active, metal-free oxygen reduction electrocatalysts for alkaline fuel cells. *Angew. Chem. Int. Ed.* **53**, 4102–4106 (2014).

54. C. Koch, Determination of core structure periodicity and point defect density along dislocations, thesis, (Arizona State University, 2002).

55. S. Hovmöller, CRISP: Crystallographic image processing on a personal computer. *Ultramicroscopy* **41**, 121–135 (1992).

56. J. Barthel, Dr. Probe: A software for high-resolution STEM image simulation. *Ultramicroscopy* **193**, 1–11 (2018).

57. A. De Backera, K. H. W. van den Bos, W. Van den Broek, J. Sijbers, S. Van Aert, StatSTEM: An efficient approach for accurate and precise model-based quantification of atomic resolution electron microscopy images. *Ultramicroscopy* **171**, 104–116 (2016).

58. G. Kresse, J. Furthmüller, Efficiency of ab-initio total energy calculations for metals and semiconductors using a plane-wave basis set. *Comput. Mater. Sci.* **6**, 15–50 (1996).

59. G. Kresse, J. Furthmüller, Efficient iterative schemes for ab initio total-energy calculations using a plane-wave basis set. *Phys. Rev. B* **54**, 11169–11186 (1996).

60. J. P. Perdew, K. Burke, M. Ernzerhof, Generalized gradient approximation made simple. *Phys. Rev. Lett.* **77**, 3865–3868 (1996).

61. P. E. Blöchl, Projector augmented-wave method. *Phys. Rev. B* **50**, 17953–17979 (1994).

62. G. Henkelman, B. P. Uberuaga, H. Jónsson, A climbing image nudged elastic band method for finding saddle points and minimum energy paths. *J. Chem. Phys.* **113**, 9901–9904 (2000).

63. Y. Wang, Z. Song, D. Ma, H. Luo, D. Liang, X. Bao, Characterization of Rh-based catalysts with EPR, TPR, IR and XPS. *J. Mol. Catal. A Chem.* **149**, 51–61 (1999).

64. D. V. Dyck, J. R. Jinschek, F.-R. Chen, 'Big Bang' tomography as a new route to atomic-resolution electron tomography. *Nature* **486**, 243–246 (2012).

65. H. A. Gasteiger, N. Markovic, P. N. Ross Jr., E. J. Cairns, Carbon monoxide electrooxidation on well-characterized platinum-ruthenium alloys. *J. Phys. Chem.* **98**, 617–625 (1994).

66. H. A. Gasteiger, N. Markovic, P. N. Ross Jr., H$_2$ and CO electrooxidation on well-characterized Pt, Ru, and Pt–Ru. 2. Rotating disk electrode studies of CO/H$_2$ mixtures at 62°C. *J. Phys. Chem.* **99**, 16757–16767 (1995).

67. H. A. Gasteiger, N. Markovic, P. N. Ross Jr., H$_2$ and CO electrooxidation on well-characterized Pt, Ru, and Pt–Ru. 1. Rotating disk electrode studies of the pure gases including temperature effects. *J. Phys. Chem.* **99**, 8290–8301 (1995).

68. H. Yin, S. Zhao, K. Zhao, A. Muqsit, H. Tang, L. Chang, H. Zhao, Y. Gao, Z. Tang, Ultrathin platinum nanowires grown on single-layered nickel hydroxide with high hydrogen evolution activity. *Nat. Commun.* **6**, 6430 (2015).

69. C. Chen, Y. Kang, Z. Huo, Z. Zhu, W. Huang, H. L. Xin, J. D. Snyder, D. Li, J. A. Herron, M. Mavrikakis, M. Chi, K. L. More, Y. Li, N. M. Markovic, G. A. Somorjai, P. Yang, V. R. Stamenkovic, Highly crystalline multimetallic nanoframes with three-dimensional electrocatalytic surfaces. *Science* **343**, 1339–1343 (2014).

70. P. Wang, K. Jiang, G. Wang, J. Yao, X. Huang, Phase and interface engineering of platinum-nickel nanowires for efficient electrochemical hydrogen evolution. *Angew. Chem. Int. Ed.* **55**, 12859–12863 (2016).

71. P. Wang, X. Zhang, J. Zhang, S. Wan, S. Guo, G. Lu, J. Yao, X. Huang, Precise tuning in platinum-nickel/nickel sulfide interface nanowires for synergistic hydrogen evolution catalysis. *Nat. Commun.* **8**, 14580 (2017).

72. K. Wang, B. Huang, F. Lin, F. Lv, M. Luo, P. Zhou, Q. Liu, W. Zhang, C. Yang, Y. Tang, Y. Yang, W. Wang, H. Wang, S. Guo, Wrinkled Rh$_2$P nanosheets as superior pH-universal electrocatalysts for hydrogen evolution catalysis. *Adv. Energy Mater.* **8**, 1801891 (2018).

73. Z. Li, Y. Feng, Y. L. Liang, C. Q. Cheng, C. K. Dong, H. Liu, X. W. du, Stable rhodium (IV) oxide for alkaline hydrogen evolution reaction. *Adv. Mater.* **32**, 1908521 (2020).

74. Z. Liu, J. Qi, M. Liu, S. Zhang, Q. Fan, H. Liu, K. Liu, H. Zheng, Y. Yin, C. Gao, Aqueous synthesis of ultrathin platinum/non-noble metal alloy nanowires for enhanced hydrogen evolution activity. *Angew. Chem. Int. Ed.* **57**, 11678–11682 (2018).

75. L. Su, Y. Zhao, F. Yang, T. Wu, G. Cheng, W. Luo, Ultrafine phosphorus-doped rhodium for enhanced hydrogen electrocatalysis in alkaline electrolytes. *J. Mater. Chem. A* **8**, 11923–11927 (2020).

76. K. Jiang, B. Liu, M. Luo, S. Ning, M. Peng, Y. Zhao, Y. R. Lu, T. S. Chan, F. M. F. de Groot, Y. Tan, Single platinum atoms embedded in nanoporous cobalt selenide as electrocatalyst for accelerating hydrogen evolution reaction. *Nat. Commun.* **10**, 1743 (2019).

77. S. Fang, X. Zhu, X. Liu, J. Gu, W. Liu, D. Wang, W. Zhang, Y. Lin, J. Lu, S. Wei, Y. Li, T. Yao, Uncovering near-free platinum single-atom dynamics during electrochemical hydrogen evolution reaction. *Nat. Commun.* **11**, 1029 (2020).

78. G. Li, C. Fu, W. Shi, L. Jiao, J. Wu, Q. Yang, R. Saha, M. E. Kamminga, A. K. Srivastava, E. Liu, A. N. Yazdani, N. Kumar, J. Zhang, G. R. Blake, X. Liu, M. Fahlman, S. Wirth, G. Auffermann, J. Gooth, S. Parkin, V. Madhavan, X. Feng, Y. Sun, C. Felser, Dirac nodal arc semimetal PtSn$_4$: An ideal platform for understanding surface properties and catalysis for hydrogen evolution. *Angew. Chem. Int. Ed.* **58**, 13107–13112 (2019).

79. F. Luo, L. Guo, Y. Xie, J. Xu, W. Cai, K. Qu, Z. Yang, Robust hydrogen evolution reaction activity catalyzed by ultrasmall Rh–Rh$_2$P nanoparticles. *J. Mater. Chem. A* **8**, 12378–12384 (2020).

Citation: Z. Zhang, G. Liu, X. Cui, Y. Gong, D. Yi, Q. Zhang, C. Zhu, F. Saleem, B. Chen, Z. Lai, Q. Yun, H. Cheng, Z. Huang, Y. Peng, Z. Fan, B. Li, W. Dai, W. Chen, Y. Du, L. Ma, C.-J. Sun, I. Hwang, S. Chen, L. Song, F. Ding, L. Gu, Y. Zhu, H. Zhang, Evoking ordered vacancies in metallic nanostructures toward a vacated Barlow packing for high-performance hydrogen evolution. *Sci. Adv.* **7**, eabd6647 (2021).